

3D Cross-Point Plasmonic Nanoarchitectures Containing Dense and Regular Hot Spots for Surface-Enhanced Raman Spectroscopy Analysis

Jae Won Jeong, Md Masud Parvez Arnob, Kwang-Min Baek, Seung Yong Lee, Wei-Chuan Shih, and Yeon Sik Jung*

With the increasing demand for rapid and accurate label-free detection tools for extremely small amount of molecules, surface enhanced Raman scattering (SERS) analysis has emerged as one of the most practical techniques.^[1–8] SERS technology is based on the plasmon resonance on the surface of metallic nanostructures, which focus incident light in the form of near-field evanescent waves. Various plasmonic nanostructures thus can amplify the probability of Raman scattering by several orders-of-magnitude.^[3,5,7,9] Previous studies reported that some strong light-focusing nanostructures contain highly effective “hot spots” that intensify the Raman signal by a factor of up to 10^{15} .^[3,10–13] Based on various SERS analysis techniques, even single-molecule detection has been realized, and diverse novel applications including in vitro and in vivo diagnosis have also been demonstrated.^[3–5,14–19] One of the most effective plasmonic nanostructures for SERS analysis is sub-10 nm narrow gap structures, where the degree of Raman signal enhancement ratio increases exponentially as the nanogap size decreases.^[20,21] However, conventional lithographic approaches for high volume manufacturing of these nanogaps are challenging due to lack of fabrication techniques that satisfy high throughput, low cost, and sufficient reproducibility.

Previously, Yoon and co-workers suggested an alternative strategy based on plasmonic coupling between vertically stacked structures.^[22] They positioned Au nanowires on top of a continuous Au film, where an excitation laser is irradiated

vertically to the plane of the metal film. Consequently, along the linear contact region, surface plasmon resonance of Au nanowires is strongly coupled with surface plasmon polaritons of the Au thin film. These results suggest that the synergic combination of a nanogap and vertical stacking may open new possibilities for ultrahigh SERS signal enhancement. However, the realization of well-controlled 3D plasmonic nanostructures is challenging with conventional top-down lithographic methods. On the other hand, solution-based synthesis and spreading of metal nanoparticles or nanowires also accompany issues such as position-dependent variation of the SERS signal and relatively poor reproducibility due to the random distribution of plasmonic nanostructures.^[15,23–25] Although multilayered nanoparticle films generated by layer-by-layer particle deposition^[24] or evaporative self-assembly^[25] provided better SERS signal homogeneity, which was obtained only when the film was sufficiently thick (up to even several micrometers), excessively high packing density of nanostructures hindered effective penetration of probe molecules into hot spots.

In this sense, nanotransfer printing (nTP) may be a more practical solution to controllably build 3D nanostructures. An nTP technique is usually composed of several steps—preparation of nanostructured elastomeric replica, deposition of functional materials, and transfer of functional nanostructures.^[26] The nanostructures can be transferred onto other substrates by contacting the mold on the surface of the receiver substrate. To overcome the issues of resolution limit (typically several tens of nm) and low transfer yield of conventional nTP, we previously developed and demonstrated that solvent-assisted nanotransfer printing (S-nTP) can controllably generate extremely fine (down to sub-10 nm) functional nanostructures with excellent transfer yield ($\approx 100\%$). Our S-nTP technology is based on the fabrication of a high-resolution master mold using block copolymer (BCP) self-assembly, the use of a bilayer thin film replica for replication, and solvent-induced debonding. In particular, we developed a gel-type elastomeric transfer medium for solvent-assisted transfer of generated nanostructures on almost any type of surface. The excellent uniformity of the printed nanostructures is another advantage of nTP, as it makes it possible to obtain highly uniform and reproducible SERS signals.

Herein, we demonstrate the realization of vertically stacked 3D cross-point plasmonic nanostructures with excellent SERS signal intensity and uniformity over a macroscopic area based on high-resolution nanotransfer printing. This 3D crossbar array is analogous to recent memory device architectures designed for maximizing information storage density

Dr. J. W. Jeong, K.-M. Baek, Prof. Y. S. Jung
Department of Materials Science and Engineering
Korea Advanced Institute of Science and
Technology (KAIST)
291 Daehak-ro, Yuseong-gu, Daejeon 305-701
South Korea
E-mail: ysjung@kaist.ac.kr

M. M. P. Arnob, Prof. W.-C. Shih
Department of Electrical and Computer Engineering
University of Houston
4800 Calhoun Road, Houston, TX 77204, USA

Dr. S. Y. Lee
Center for Materials Architecturing
Korea Institute of Science and Technology (KIST)
Hwarangno 14-gil 5, Seongbuk-gu, Seoul 136-791, South Korea

Dr. J. W. Jeong
Powder Technology Department
Korea Institute of Materials Science (KIMS)
Changwon 641831, South Korea



DOI: 10.1002/adma.201602603

and improving device performance.^[27,28] For more facile and rapid stacking of multilayer nanostructures, we developed and applied a second-generation S-nTP technique based on a multipurpose single-layer replica without using an additional transfer-medium, thereby significantly simplifying the overall nTP steps and enabling the prompt repetition of nTP for multilayer stacking of nanowires. We report that sequentially transfer-printed sub-20 nm nanowires can provide both an in-plane coupling effect in the nanogap region and an out-of-coupling effect at the cross-points where two nanowires are closely stacked, achieving excellent enhancement of Raman signals from probed molecules with an average enhancement factor of $\approx 4.1 \times 10^7$ depending on structural and material parameters. Moreover, nanowires-on-film hybrid structures obtained by sequential printing on a continuous metal film show highly intensified SERS signals due to vertical plasmonic coupling between the upper nanowires and the underlying film.

In most SERS analyses, SERS substrates are disposed of after one-time analysis to avoid any contamination from previous tests. Therefore, reducing the fabrication cost is one of the most important requirements for practical SERS substrates while assuring sufficiently high signal enhancement ratios. As mentioned above, we previously demonstrated a novel S-nTP process having a resolution as low as 8 nm by employing a high-modulus polymer thin film replica and a solvent-vapor-assisted adhesion switching principle using a polymer gel pad as a solvent-injection medium. However, further simplification of S-nTP would be advantageous for more facile and rapid generation of multilayer stacks of nanowires. In the present study, we realized the direct transfer of nanostructures from a polymethylmethacrylate (PMMA) replica to a receiver substrate, as shown in Figure S1 in the Supporting Information. The key advancement of the second-generation (2G) S-nTP is the use of the single-layer PMMA replica (shown in Figure S2, Supporting Information) attached on a polyimide (PI) adhesive film, which can also serve as a high-yield transfer medium, eliminating the need of an additional transfer medium (previously PDMS gel) and a transfer step.

By carefully controlling the deposition parameters of metals, different morphologies of nanostructures can be formed and their dimensions can be controlled systematically. For example, we present that, depending on the deposition rate, the film thickness, and the angle between the substrate and the direction of deposition, either continuous nanowires or discrete head-to-tail nanorod arrays can be obtained. With a high deposition rate ($>0.1 \text{ nm s}^{-1}$) and a large deposition angle ($>80^\circ$), continuous nanowires were formed, as shown in Figure 1a–d. However, at a low deposition rate and a small deposition angle, discrete “head-to-tail” nanorods with a relatively small length-to-width ratio were generated, as depicted in Figure 1e–h. This is attributed to the formation of larger grains resulting from a longer diffusion distance of adatoms during the initial stage of thin film growth.^[29] Notably, the average gap distance between the head-to-tail nanorods along the axis direction was about 5 nm, suggesting that these small gaps act as highly effective hot spots for significant SERS signal enhancement. The results of the statistical evaluation of the nanogap size and distribution are provided in the Supporting Information. The morphology of the nanostructures, and the related geometrical variables depending

on deposition parameters are also summarized in Table S1 of the Supporting Information. We also obtained the absorption spectra of Au nanowires and nanorods in the range of visible-infrared (Figure 1i). Plasmonic resonance occurred at the wavelength (λ) of $\approx 580 \text{ nm}$ for Au nanowires, and the resonance peak was significantly broadened for Au nanorods due to the additional rod-to-rod coupling (occurring for $\lambda \sim 600\text{--}800 \text{ nm}$), which is supported by the large variations in the length of nanorods.^[30]

In order to characterize the SERS performance of the printed 2D nanostructures, the nanostructure surface was decorated with rhodamine 6G (R6G) molecules. (SERS peak positions of R6G are listed in Table S2, Supporting Information.) Ethanol solution (27 μL) of R6G with a concentration of 10^{-6} M was dropped on the Au nanowire or nanorod arrays to cover the whole area of 1 cm^2 , and the Raman measurement was performed after the solvent dried. Clear SERS spectra in Figure 1j present ≈ 3 times higher signal intensity for the discrete head-to-tail Au nanorods compared to the continuous counterpart. By assuming the nanorods have a cylindrical shape, the portion of the sub-5 nm nanogap surface region is only 6%, which suggests that the sub-5 nm nanogap structures have ≈ 34 times higher signal enhancement factor compared to other wider nanogap surfaces in the 2D array.

While the SERS signal enhancement mechanism of the monolayer Au nanostructures is related to the coupling in the in-plane direction, the synergic combination of horizontal and vertical coupling effects in 3D plasmonic nanostructures would provide more significant enhancement of Raman signals. One strong advantage of our S-nTP is that it allows rapid, repeated, and scalable printing of high-resolution nanostructures on the same substrate because it can be implemented regardless of the surface topology and surface energy of the receiver substrates. The aligned 1D nanowires and nanorods are suitable for use as building blocks for the formation of unique 3D cross-point nanostructures (3D-CPN) for SERS analysis because ultra-small nanogaps are formed at the cross-points, where lower and upper layers are closely spaced. Moreover, the empty space (i.e., pores) in the 3D-CPN is continuously connected, which would allow facile penetration of solutions containing analytes.

The schematic in Figure 2a,b shows the procedure for fabricating 3D-CPN through the sequential S-nTP process. The first layer of the Au nanowire arrays is transferred onto a Si substrate, and the second layer is printed on top of the first layer with an alignment angle of 90° . Through successive printing of the nanowire array, multistacked 3D crossed-wire nanostructures with various number of layers can be fabricated. Highly porous 3D-stacked structures without any residual polymers can be confirmed from the top-down and cross-section scanning electron microscopy (SEM) images in Figure 2c. We then examined the SERS characteristics of the 3D-CPN. As depicted in Figure 2f, the intensity of the Raman spectra of 4-ATP and R6G linearly increased up to five layers of stacking. Importantly, for the same total amount of R6G molecules dropped on the multilayer Au nanostructures, the resulting SERS signal increased as the number of layers increased, suggesting much higher signal enhancement for the multilayer structures than the 2D array. For example, the SERS signal from the five-layer sample was ≈ 10.8 times stronger than that from the monolayered 2D

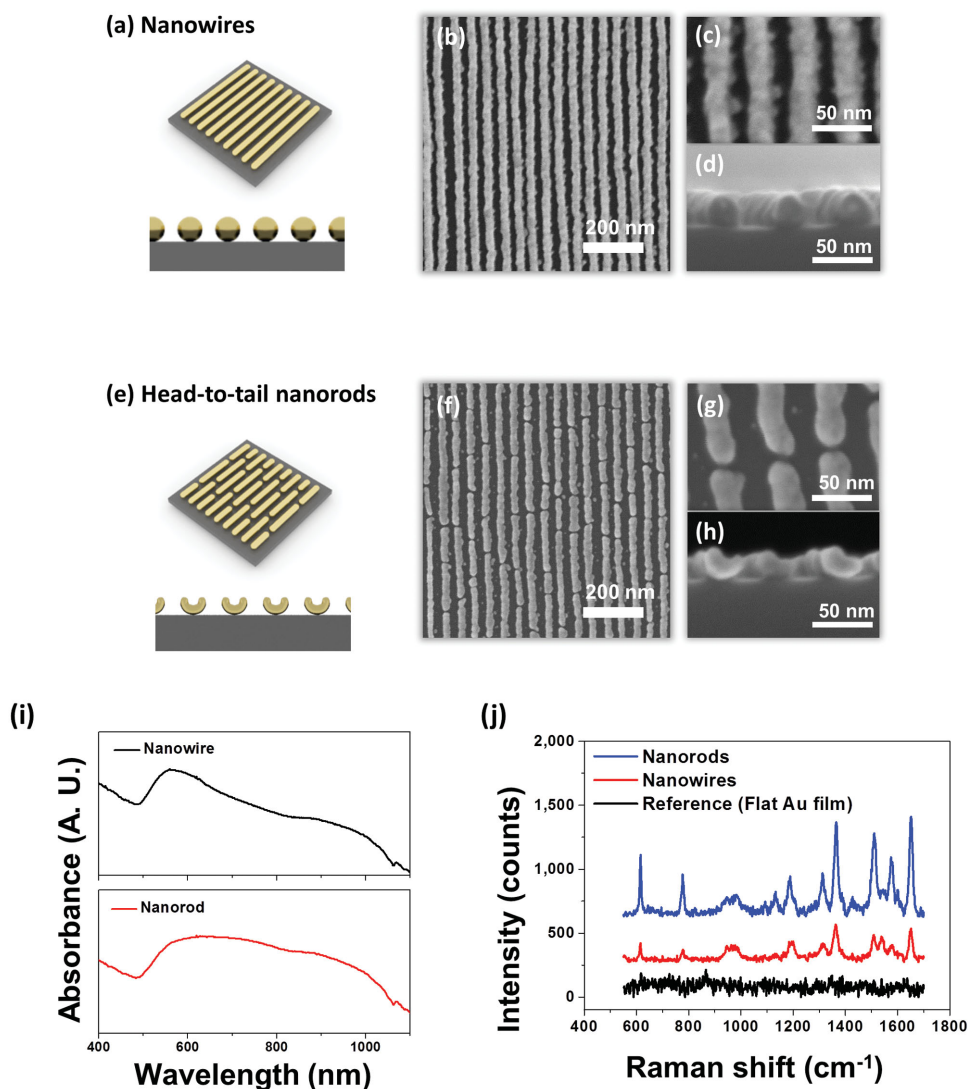


Figure 1. Controlled morphology of printed nanostructures and SERS characterization results. a) A schematic of continuous Au nanowires. b,c) Top-down SEM images of continuous Au nanowires with a low (b) and high magnification (c). e) A schematic of printed Au nanorods with a “head-to-tail” arrangement. f,g) Top-down SEM images of Au nanorods with a low (f) and high magnification (g). h) Cross-section SEM image of Au nanowire. i) Visible-near infrared absorption spectra of Au nanowires and nanorods. j) SERS signals obtained from the R6G-decorated Au nanowires, Au nanorods, and flat Au film.

arrays. The high SERS signal enhancement can be explained by the fact that more stacking of nanostructures would provide additional hot spots, inducing strong plasmonic coupling along the vertical direction.^[22,31,32] However, the intensity decreased (R6G) or remained almost constant (4-ATP) for more than five layers. This can be explained by the finite penetration depth of the laser beam into the 3D nanostructures. As shown in Figure 2d, the transmittance of 3D-CPN decreases dramatically as the number of stacking layers increases. The intensity of the incident light continuously decreases as it penetrates into the 3D-CPN. Considering the fact that the SERS signals from the molecules should also penetrate an equal depth to escape from the structure and to be counted by the detector, it is reasonably understood that there is a maximum depth that the incident light can penetrate, and from which Raman-scattered photons can escape from the structure to be collected by the detectors.

Moreover, in the case of R6G, the amount of molecules per area decreases for “thicker” 3D-CPN because the same amount of R6G molecules was dropped and distributed over the entire surface area. This would decrease the effective quantity of molecules on the near-surface region, where the contribution to the SERS signal intensity is relatively more significant. On the other hand, the saturation of SERS intensity for 4-ATP can be understood by the formation of uniform monolayer molecules on the whole surface throughout the entire depth, because the 4-ATP molecules were cast on the nanostructure surface for binding and then washed with solvent to remove unreacted molecules.

The SERS characteristics of the 3D-CPN can be better clarified by simulating the electric field (e-field) distribution across the 3D network. Figure 3a–f depicts the simulated e-field enhancements (excited field, $E/\text{incident field}$, $E_0 = 1 \geq 1$) for

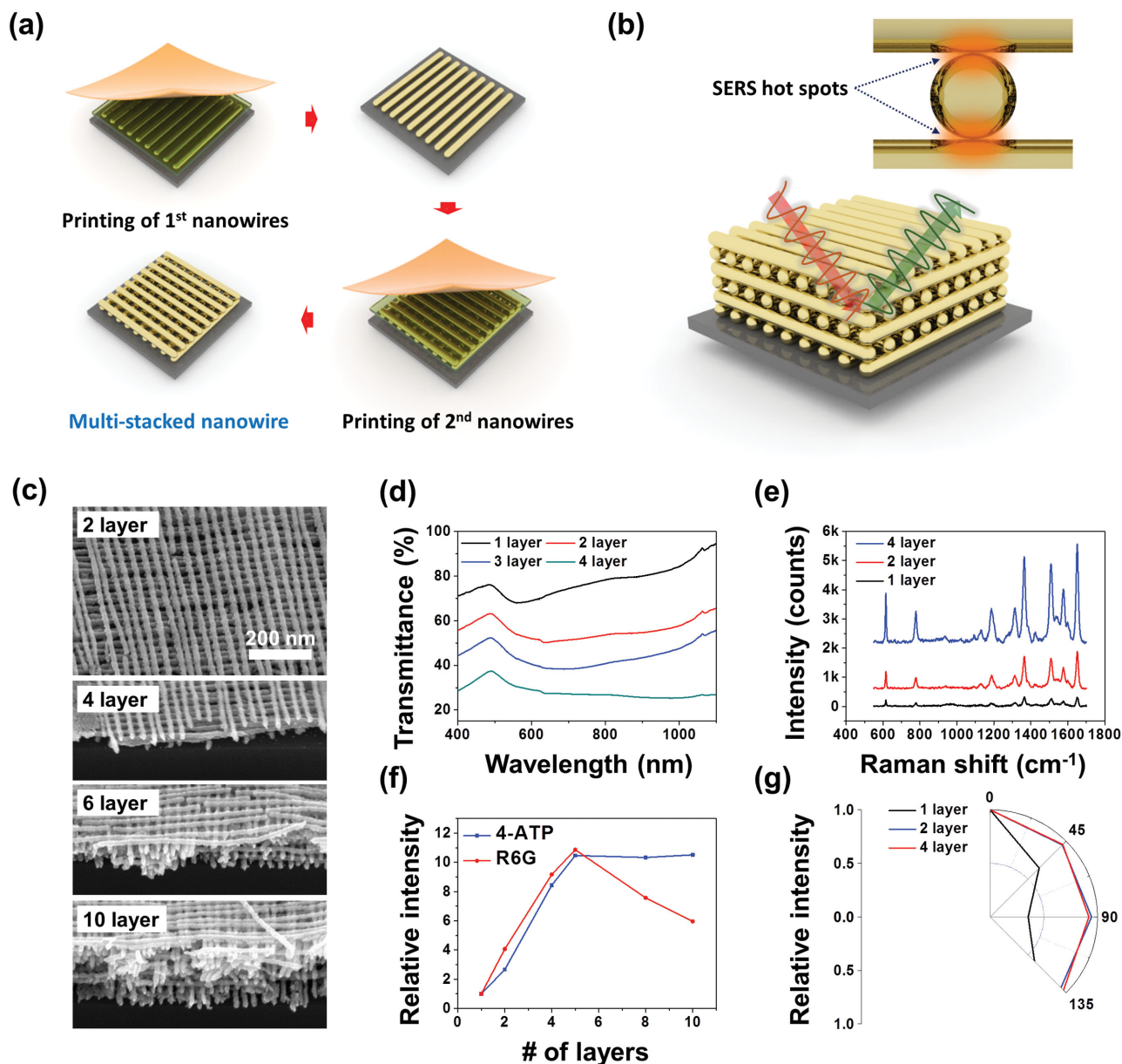


Figure 2. 3D cross-point plasmonic nanostructures (3D-CPN) and SERS characterization results. a) Schematic procedure for the fabrication of 3D-CPN. b) A schematic of fabricated 3D-CPN. c) top-down and cross-section SEM images of 3D-CPN with various numbers of layers. d) Transmittance spectra of Au 3D-CPN with an increasing number of stacked layers. e) SERS signals obtained from R6G-decorated Au 3D-CPN. f) Relative SERS signal intensity depending on the number of stacked layers. Relative SERS intensity of R6G and 4-ATP molecules occurring at 1650 and 1080 cm⁻¹, respectively, was used for the analysis. g) Angle-dependency of monolayer Au nanowires and 3D-CPN. Relative SERS intensity of R6G at 1650 cm⁻¹ was used for the analysis.

3D-CPN of different numbers of stacking layers: 1, 2, 4, 5, 8, and 10, respectively. We note that the maximum field enhancement occurs at the cross-points of the stacking layers due to the presence of nanogaps.^[33] The hot spots are regularly distributed, which ensures very repeatable SERS measurements. Figure 3g shows the maximum e-field enhancement variation with respect to the number of stacking layers. All the calculations are based on the finite difference time domain (FDTD) method and for 514 nm excitation wavelength. (Simulation results for 633 and 785 nm excitation wavelength are also

depicted in Figure S3, Supporting Information.) Figure 3h presents the simulation set-up. The orthogonal nanowires are piled up along the z-direction. The incident wave is polarized along the x-direction and the 2D e-field monitor is placed in the x-z plane at the cross-points of the nanowires. As shown in Figure 3g, the maximum e-field enhancement increases up to five layers of stacking. However, for 8 and 10 stacking layers, the e-field enhancement is smaller than that for 5. The maximum field enhancement is similar for 8 and 10 layers of stacking. The irregular e-field enhancement can be attributed

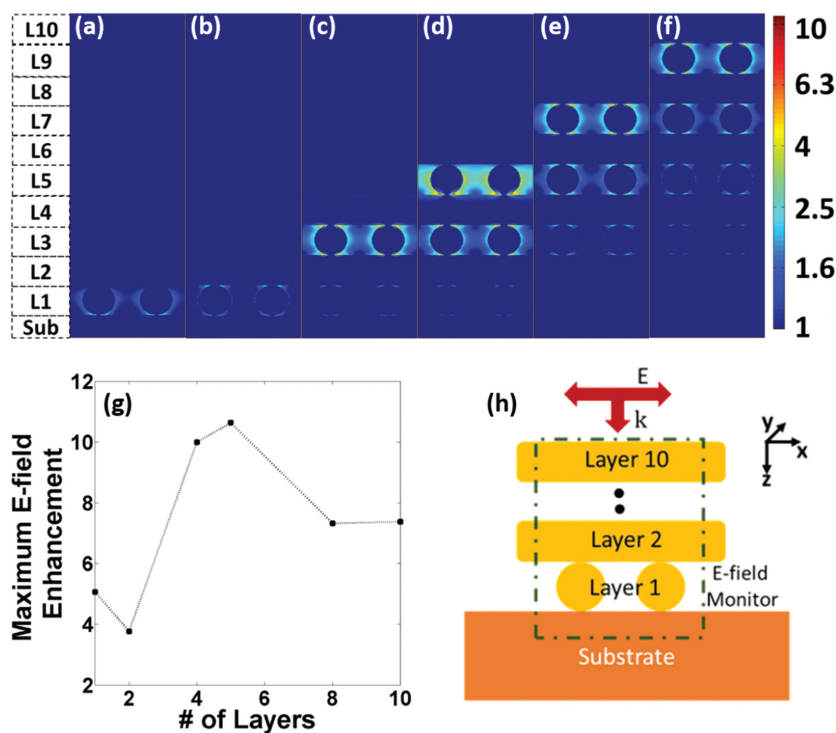


Figure 3. Electric field enhancement ($E/E_0 \geq 1$) for 3D CPN at 514 nm wavelength: a) layer 1, b) layer 2, c) layer 4, d) layer 5, e) layer 8, and f) layer 10. g) Maximum e-field variation with respect to different stacking layers. h) Simulation set-up.

to the interference of waves propagating back and forth across the stacking layers.^[34] The interference might be constructive or destructive, which affects the local field enhancement across the 3D network. It may not be straightforward to directly correlate the measured SERS intensity with the maximum field enhancement ratio of a local point because the total Raman intensity is the integrated sum of the contributions from various hot spots. However, considering that the (experimentally measured) minimum number of Au nanowire layers providing the highest SERS intensity is 5, as shown in Figure 3f, these results suggest that the hot spots formed at the junctions between the topmost and the second-layer nanowires play the most significant role.

The multistacking of nanowires was also advantageous in reducing angle-dependent signal variation, introduced by structural anisotropy. Because the incident laser was uniaxially polarized in the Raman measurement, the SERS intensity varies depending on the angle between the long axis of the nanowires and the laser polarization direction in the case of a 2D array of nanowires. Interestingly, such angle dependency can be significantly lowered for 3D-CPN structures, as presented in Figure 2g. An almost identical SERS intensity was obtained for the 3D-CPN structures regardless of the angle between nanowires and laser polarization axis.

Analogous signal enhancement through the vertical stacking of nanostructures was also confirmed for Ag. It is well known that the SERS signal enhancement of Ag nanostructures is more significant than that of Au nanostructures due to the difference in the dielectric constant.^[7,35] We fabricated silver-based 3D-CPN through the deposition of Ag on the PMMA replica.

Approximately 100-fold enhancement of the SERS signal intensity was observed for Ag nanorod arrays compared to the Au counterpart. The trace amount detection capability of the printed nanostructures was also investigated. Raman spectra of R6G molecules were clearly recognized at an extremely low concentration of 10^{-10} and 10^{-11} M, which corresponds to 16 and 1.6 molecules μm^{-2} , respectively (Figures S4 and S5 and Table S2, Supporting Information). Because fewer than two molecules exist within the laser spot size ($= 1 \mu\text{m}^2$) for the 10^{-11} M solution, nearly single-molecule detection capability of our printed Ag nanostructures was confirmed.

Another promising structure that can boost the vertical plasmonic coupling to a great extent is the combination of periodic nanostructures and a flat film. It has been suggested on a theoretical basis that the coupling between the localized surface plasmons from an upper layer of plasmonic nanostructures and the surface plasmon polaritons (SPP) of an underlying metal film enable the multiplicative intensity enhancement effect.^[19,31] While uniform formation of this structure on a macroscopic area is challenging with conventional top-down lithography methods and solution-based casting of nanoparticles, S-nTP can also generate

such hybrid structures with an excellent degree of alignment in a simple and rapid manner. As schematically shown in Figure 4a, nanowires and nanorods could be directly printed on flat Au or Ag films. The SERS characteristics of the nanorod-on-film hybrid structures were evaluated after dropping a 10^{-6} M R6G solution. Interestingly, the intensity of the SERS signals obtained from single-layer Ag nanorods on an Ag film was even higher than that of a two-layer cross-point Ag nanorod structure on a Si substrate and comparable with that of four-layer 3D-CPN (Figure 4b). These results suggest that the light focusing effect due to the vertical coupling between LSPR and SPP can be more significant than that occurring from the vertical LSPR coupling between nanostructures.

Furthermore, when one more layer was transfer-printed onto the structure (i.e., two-layer cross-point Ag nanorods on Ag film), the signal intensity was further enhanced, which can be understood from the additional coupling effect from the crossed points. However, interestingly, when more layers were stacked, the measured SERS spectra were significantly weakened. As shown in Figure 4b and Table S3 of the Supporting Information, the two-layer Ag nanorod array on the Ag film showed the highest SERS signal intensity. The SERS intensity of four-layer 3D-CPN on the Ag film was almost analogous to that formed on the Si substrate (Table S3, Supporting Information). The total SERS intensity was not meaningfully influenced by the existence of the bottom metal film in the case of the thicker 3D-CPN, also confirming the limited penetration depth of the laser beam into the 3D nanostructures. The two-layer CPN on the Ag film showed reasonable areal uniformity.

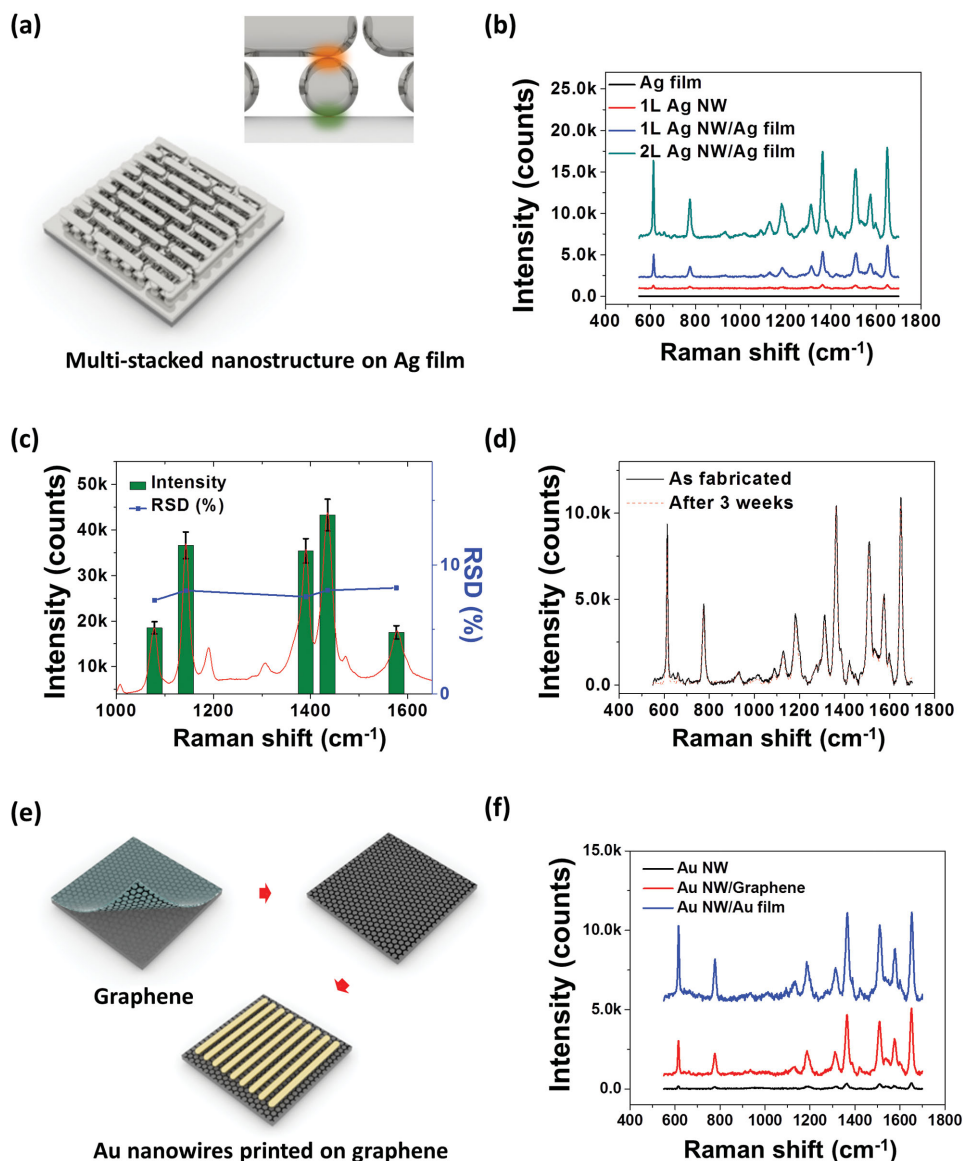


Figure 4. Nanostructure-on-film hybrid SERS structures and SERS characterization results. a) Schematic describing multilayered Ag nanorods (3D-CPN) on Ag film. b) SERS signals obtained from R6G-decorated hybrid nanostructures, nanorods, and flat metal film. (Laser power: 0.31 mW.) c) Large-area uniformity of hybrid SERS nanostructures coated with 4-ATP molecules. Relative standard deviation (RSD) values were calculated from 30 random spots within the total area of $1.5 \times 1.5 \text{ cm}^2$. d) Long-term stability test of the hybrid SERS structures: The SERS signal of R6G-decorated hybrid structures was obtained immediately after device fabrication and after keeping the sample in ambient conditions for three weeks. e) Schematic procedure for the fabrication of graphene-Au nanowire hybrid SERS structures. f) SERS signals of R6G molecules obtained from graphene/Au nanowires and monolayer Au nanowires alone.

The relative standard deviation (RSD) of the SERS signal intensity from 30 random spots of the hybrid SERS substrate was about 7.2%–8.2% for 4-ATP and 8.2%–9.8% for R6G molecules, respectively. (Figures 4c and Figure S9, Supporting Information). The sample-to-sample variation in SERS signal intensity was also less than 9%, as demonstrated in Figure S10 of the Supporting Information. The long-term signal stability of the hybrid structure was also evaluated. As depicted in Figure 4d, the Ag-based hybrid structure showed almost invariant SERS spectra even after storage in ambient conditions for three weeks. As previous research suggests,^[36] controlling the side-wall profile of the component nanowires in the 3D-CPN

to further improve its enhancement factor remains promising future research.

We quantitatively evaluated average enhancement factors (AEFs) of the cross-point plasmonic nanostructures. AEF values quantitatively indicate the degree of Raman signal enhancement and thus are related to the detection limit of SERS measurement. For the experimental determination of the AEF, we compared the SERS signals from the 3D nanostructures with those of ordinary Raman signals of probe molecules. To obtain the Raman signals as a reference, R6G was solution-cast on a Si substrate to form a R6G film (Figure S11, Supporting Information).^[37] The AEF can then be estimated using the following equation^[12]

$$AEF = (I_{\text{SERS}} \times N_{\text{Film}}) / (I_{\text{Normal}} \times N_{\text{SERS}}) \quad (1)$$

where I_{SERS} , N_{SERS} , I_{Normal} , and N_{Film} represent the intensity of the SERS signal, the intensity of the Raman signal, the number of molecules on the SERS substrate, and the number of molecules of the R6G film on the Si wafer, respectively. Details of the AEF evaluation process can be found in the Supporting Information. The AEF values showed a large variation depending on the various 2D or 3D geometries of the nanostructures. An AEF of 5.2×10^3 was obtained from a monolayer 2D Au nanowire array, while the monolayer Ag head-to-tail nanorods showed an AEF of 1.7×10^6 . When the nanostructures were vertically stacked up to four layers, the AEF increased to 4.9×10^4 and 1.5×10^7 for Au nanowires and Ag nanorods, respectively. Importantly, the maximum AEF of 4.1×10^7 , which allows single-molecule detection,^[12] was obtained for two-layer Ag nanorods on a continuous Ag film. This is comparable with the highest AEF values reported thus far.^[12,38–42] The unique advantage of our approach is the alignment of such hot spots with high density and regularity, even in 3D. Moreover, the degree of signal enhancement and the uniformity of our printed SERS substrate were superior to a commercially available SERS substrate (Figures S12 and S13, Supporting Information).

Recently, significant Raman enhancement through the combination of 2D materials and plasmonic metallic nanostructures has been reported.^[43–49] In addition to strong light focusing by plasmonic nanostructures, charge transfer from 2D materials additionally enhances Raman signals. For example, nanostructure-graphene hybrid materials can greatly enhance the Raman signal.^[43–46] Our S-nTP is highly useful in the fabrication of such hybrid nanostructures. As an example, an Au-nanowire/graphene hybrid structure was fabricated through one-step printing of plasmonic Au nanowires on few-layer graphene. As shown in Figure 4e,f, the graphene-nanowire hybrid structure showed 11-fold enhanced Raman intensity relative to the 2D nanowire array without graphene.^[19,43,50] From these results, we expect that S-nTP can potentially realize more complex 3D sensing nanostructures by combining various building blocks with specific binding properties and signal-enhancement capabilities.

SERS analysis can provide rapid and label-free identification as well as quantification of diverse molecules and can be highly useful in biosensing for diagnosis and healthcare monitoring.^[51,52] In particular, the real-time SERS monitoring of the glucose level in blood has been successfully demonstrated.^[53–55] Although a high fasting glucose level in blood is a sign of diabetes, due to the inconvenience and infection risk of blood tests, noninvasive and in situ monitoring of glucose levels in humans or animals has been extensively attempted.^[56–58] It should be noted that glucose is present not only in the blood but also in tears,^[59] and thus accurate monitoring of the glucose level in human tears by employing contact-lens-type sensor can be an alternative approach for noninvasive glucose monitoring.

We demonstrate the versatility of our S-nTP for unconventional application of SERS by demonstrating a “SERS contact lens”, which can potentially enable in situ detection of glucose levels in tears. Our S-nTP can generate highly uniform SERS structures even on a contact lens having a curved surface. The SERS lens was simply fabricated by printing Ag nanorods on

commercially available contact lenses, as schematically shown in Figure 5a. A monolayered nanorod array with an AEF 1.6×10^6 was used for the detection of aqueous glucose in the concentration range from 10^{-1} to 10^{-4} M. The fabricated SERS lens was incubated in a 1×10^{-3} M ethanol solution of decanethiol (DT) to form a uniform self-assembled monolayer of DT, which could act as a partition layer during in situ glucose analysis.^[54] Figure 5b shows a photograph of the fabricated SERS contact lens. We also printed Ag nanostructures on a soft contact lens made of hydrogel (Figure 5c). To demonstrate its glucose detection function, we mounted the SERS lens on an artificial glass eye (Figure 5d), and released one drop of 1×10^{-3} M aqueous glucose solution (which corresponds to the glucose level in the tears of diabetes patients).^[59] The graph in Figure 5e shows the obtained SERS signal before and after dropping the glucose solution. The signature Raman peaks including those at 1368 and 1465 cm^{-1} of glucose molecules were clearly detected. The detection capability of glucose with various concentrations in a range from 0.1×10^{-3} to 10×10^{-3} M is presented in Figure S14 of the Supporting Information. However, the statistical quantification was not successful due to the significant overlap of the main SERS peaks of glucose with those of the 1-DT monolayer (at 1129, 1430, and 1451 cm^{-1}). We expect that the adoption of other SAMs which have a higher binding affinity with glucose can enhance the reliability of glucose detection.^[53] Alternatively, an indirect detection method using a Raman-active self-assembled monolayer (SAM), whose SERS intensity systematically changes as it binds with glucose, can provide more reliable and systematic data for the quantitative detection of glucose.^[60] For practical applications of the SERS contact lens, demonstrating the applicability of retina-safe laser excitation and providing a proper guidance also remain important tasks.^[61] In addition to the SERS contact lens presented in this study, the versatile printing capability of our S-nTP applicable on diverse surfaces would be able to realize unique SERS platforms that can provide superior convenience and accuracy of measurement.

In summary, we have demonstrated highly SERS-active and uniform 3D cross-point plasmonic nanostructures over a large area based on solvent-assisted high-resolution nanotransfer printing. We employed nanoscale block copolymer patterns as master templates, and fabricated uniformly arranged 3D plasmonic nanostructures through pattern replication, deposition of materials, and solvent-assisted transfer printing. In particular, the sequential implementation of this ultrahigh-resolution nanotransfer printing realized fast and high-yield construction of 3D-stacked structures, where high-density crossed points serve as hot spots for huge SERS signal enhancement. Moreover, unconventional hybrid nanostructures such as nanowire-on-film and nanowire-on-graphene structures can also be controllably generated for significant SERS signal enhancement. We successfully demonstrated a high-performance, uniform, and low-cost SERS substrate with an average enhancement factor of up to 4.1×10^7 . Moreover, S-nTP enabled the fabrication of a SERS contact lens that can detect glucose in an aqueous solution. These promising results suggest that S-nTP can be extensively utilized for various nanoscale sensing platforms where registration of high-resolution nanostructures is necessary and the application of conventional lithography techniques is challenging.

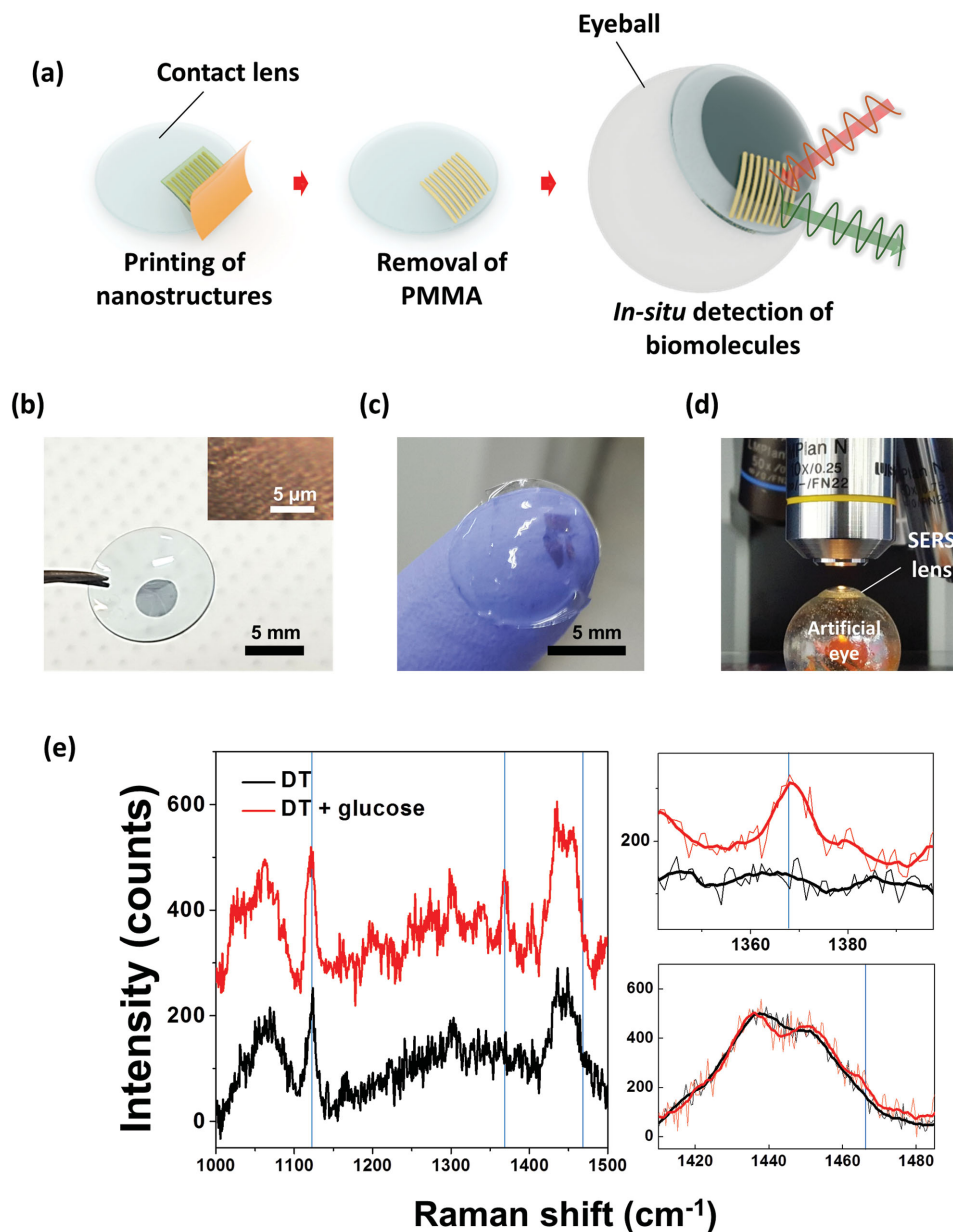


Figure 5. Fabrication of SERS contact lens and demonstration of glucose detection. a) Schematic procedure for the fabrication of SERS contact lens via transfer printing. b,c) Optical images of hard lens (b) and soft lens (c) with printed Ag nanorods. d) Measurement set-up for the SERS signal of glucose. e) Comparison of SERS spectra before and after dropping glucose solution, showing the successful detection of glucose.

Experimental Section

Fabrication of Sub-20 nm Master Template: PS-*b*-PDMS BCPs with M.W. of 48 kg mol⁻¹, which form 25 nm wide lines, were purchased from Polymer Source Inc. (Canada) and used without purification. The BCPs were dissolved in a mixed solvent of toluene, heptane, and PGMEA (1:1:1 by volume), yielding a 0.8 wt% polymer solution. Surface-patterned Si substrates with a width of 1 μm, a depth of 40 nm, and a period of 1.25 μm were used as guiding templates. The substrate was treated with a PDMS brush (5 kg mol⁻¹, Polymer Source Inc.) at 150 °C using a vacuum oven. A solution of BCP was spin-cast onto the template and was annealed for 12 h in the chamber at RT using toluene vapor. In order to remove the top-segregated PDMS layer and organic block (PS), the samples were etched by CF₄ plasma (etching time = 20 s, gas flow

rate = 30 sccm, working pressure = 15 mTorr, and plasma source power = 50 W) followed by O₂ plasma (etching time = 30 s, gas flow rate = 30 sccm, working pressure = 15 mTorr, and plasma source power = 60 W).

Formation of Plasmonic Nanostructures Via Solvent-Assisted Nanotransfer Printing: Prior to the replication, the surface of the master mold was treated with a PDMS brush (Polymer Source Inc.). PMMA (M.W. = 100 kg mol⁻¹) was purchased from Sigma-Aldrich Inc. and was dissolved in a mixed solvent of toluene, acetone, and heptane (4.5:4.5:1 by volume) to yield 4 wt% solutions. The solution was spin-cast onto the master mold with a spin speed of 4000 rpm. A polyimide adhesive film (3M Inc.) was then attached onto the surface of the polymer replica. By removing the adhesive film from the mold, the replica with an inverted image of the surface topography of the master mold was detached from the mold. Plasmonic nanostructures were formed through glancing-angle

deposition of Au (or Ag) onto the polymer replica using a thermal evaporator. The deposition angle from the substrate surface normal was modulated and optimized between 60° and 80°. Acetone/heptane vapor was applied to the polymer replica film by placing the replica/adhesive film into a solvent saturated chamber that was preheated to 45 °C. After 30 s, the adhesive film was removed from the chamber and brought into contact with the Si substrate. Mild pressure was applied for uniform contact between the nanowire/replica/adhesive film and the substrate. The adhesive film was selectively detached from the substrate while the nanostructure/replica remained on the receiver substrate. Uniformly arranged nanowires on the Si substrate can then be obtained by washing away the polymer replica film using acetone or toluene.

Raman Measurement: Rhodamine 6G (R6G) and 4-ATP were purchased from Sigma-Aldrich. Inc. and dissolved in ethanol to prepare a solution with a concentration of 10^{-6} to 10^{-11} M. Samples for SERS characterization were prepared by dipping the nanowire-printed substrate in the 4-ATP solution followed by washing using ethanol. R6G solution was drop-cast on the plasmonic nanostructures and was dried. The Raman scattering signal was collected for 1–30 s using a dispersive Raman microscope (ARAMIS, Horiba) equipped with a 514 nm Ar-ion laser. Additional details of the experimental conditions used in the Raman measurement are described in the Supporting Information. For the observation and analysis of the samples, a field emission scanning electron microscope (FE-SEM, Hitachi S-4800) with an acceleration voltage of 15 kV and a working distance of 5 mm was used.

Finite-Difference Time-Domain (FDTD) Simulation: The 3D FDTD simulations were done for six different numbers of stacking layers of the nanowires: 1, 2, 4, 5, 8, and 10. The simulation domain varied from $98.2 \text{ nm} \times 98.2 \text{ nm} \times 3528 \text{ nm}$ to $98.2 \text{ nm} \times 98.2 \text{ nm} \times 4272 \text{ nm}$ depending on the number of layers. Each layer contained two nanowires and the length was extended along the x or y-direction. The periodicity and infinite extent of the nanowires were realized by periodic boundary conditions (PBCs) on the x- and y-directions. Perfectly matched layers (PMLs) were used on the z-axis boundaries, which caused a larger z-simulation domain to avoid energy absorption of the evanescent field from the nanowires. The nanowires were placed on a Si substrate ($200 \text{ nm} \times 200 \text{ nm} \times 2000 \text{ nm}$) and illuminated by a plane wave source (e-field amplitude is 1) shone from the air side toward the substrate direction (z-axis). The polarization of the incident wave was along the width (x-direction) of the first nanowire layer. The e-field distribution was recorded by placing a monitor in the x–z plane at the cross-points of the orthogonal stacking layers. The effect of staircase approximation was addressed by reducing the mesh size around the nanowires to $0.5 \text{ nm} \times 0.5 \text{ nm} \times 0.1 \text{ nm}$. The reduced mesh size region varied from $130 \text{ nm} \times 130 \text{ nm} \times 128 \text{ nm}$ to $130 \text{ nm} \times 130 \text{ nm} \times 372 \text{ nm}$ depending on the number of stacking layers. Both the source and e-field monitor were placed inside the reduced mesh size region to obtain high resolution data points. The simulation times ranged from 5 to 48 h and the total memory occupancy ranged from 4 to 24 GB, with increasing time and memory according to a larger number of stacking layers. The simulations were performed on a computer with eight-core calculation nodes, each carrying 4 GB memory.

Supporting Information

Supporting Information is available from the Wiley Online Library or from the author.

Acknowledgements

This work was supported by the Center for Integrated Smart Sensors, funded by the Ministry of Science, ICT & Future Planning as Global Frontier Project (CISS-2011-0031848). This research was also supported by Basic Science Research Program through the National Research Foundation of Korea (NRF-2013R1A1A2061440) and by Open Innovation

Lab Project from National Nanofab Center (NNFC). This work was supported by the National Science Foundation (NSF CBET-1605683).

Received: May 16, 2016

Revised: July 4, 2016

Published online: August 11, 2016

- [1] D. L. Jeanmaire, R. P. Van Duyne, *J. Electroanal. Chem.* **1977**, *84*, 1.
- [2] M. G. Albrecht, J. A. Creighton, *J. Am. Chem. Soc.* **1977**, *99*, 5215.
- [3] K. A. Willets, R. P. Van Duyne, *Annu. Rev. Phys. Chem.* **2007**, *58*, 267.
- [4] N. B. Colthup, L. H. Daly, S. E. Wiberley, *Introduction to Infrared and Raman Spectroscopy*, 3rd ed., Academic Press, Boston **1990**.
- [5] A. P. Craig, A. S. Franca, J. Irudayaraj, *Annu. Rev. Food Sci. Technol.* **2013**, *4*, 369.
- [6] W. H. Yang, J. Hulteen, G. C. Schatz, R. P. Van Duyne, *J. Chem. Phys.* **1996**, *104*, 4313.
- [7] P. L. Stiles, J. A. Dieringer, N. C. Shah, R. R. Van Duyne, *Annu. Rev. Anal. Chem.* **2008**, *1*, 601.
- [8] K. Kneipp, H. Kneipp, I. Itzkan, R. R. Dasari, M. S. Feld, *Curr. Sci. India* **1999**, *77*, 915.
- [9] B. Sharma, R. R. Frontiera, A. I. Henry, E. Ringe, R. P. Van Duyne, *Mater. Today* **2012**, *15*, 16.
- [10] T. T. B. Quyen, C. C. Chang, W. N. Su, Y. H. Uen, C. J. Pan, J. Y. Liu, J. Rick, K. Y. Lin, B. J. Hwang, *J. Mater. Chem. B* **2014**, *2*, 629.
- [11] T. T. B. Quyen, W. N. Su, C. H. Chen, J. Rick, J. Y. Liu, B. J. Hwang, *J. Mater. Chem. B* **2014**, *2*, 5550.
- [12] E. C. Le Ru, E. Blackie, M. Meyer, P. G. Etchegoin, *J. Phys. Chem. C* **2007**, *111*, 13794.
- [13] D. K. Lim, K. S. Jeon, J. H. Hwang, H. Kim, S. Kwon, Y. D. Suh, J. M. Nam, *Nat. Nanotechnol.* **2011**, *6*, 452.
- [14] B. H. Liu, G. M. Han, Z. P. Zhang, R. Y. Liu, C. L. Jiang, S. H. Wang, M. Y. Han, *Anal. Chem.* **2012**, *84*, 255.
- [15] J. F. Li, Y. F. Huang, Y. Ding, Z. L. Yang, S. B. Li, X. S. Zhou, F. R. Fan, W. Zhang, Z. Y. Zhou, D. Y. Wu, B. Ren, Z. L. Wang, Z. Q. Tian, *Nature* **2010**, *464*, 392.
- [16] K. Ma, J. M. Yuen, N. C. Shah, J. T. Walsh, M. R. Glucksberg, R. P. Van Duyne, *Anal. Chem.* **2011**, *83*, 9146.
- [17] B. H. Gu, C. M. Ruan, W. Wang, *Appl. Spectrosc.* **2009**, *63*, 98.
- [18] X. X. Han, L. Chen, W. Ji, Y. F. Xie, B. Zhao, Y. Ozaki, *Small* **2011**, *7*, 316.
- [19] J. Qi, J. Zeng, F. Zhao, S. H. Lin, B. Raja, U. Strych, R. C. Willson, W.-C. Shih, *Nanoscale* **2014**, *6*, 8521.
- [20] H. X. Xu, E. J. Bjerneld, M. Kall, L. Borjesson, *Phys. Rev. Lett.* **1999**, *83*, 4357.
- [21] J. Qi, P. Motwani, M. Gheewala, C. Brennan, J. C. Wolfe, W.-C. Shih, *Nanoscale* **2013**, *5*, 4105.
- [22] I. Yoon, T. Kang, W. Choi, J. Kim, Y. Yoo, S. W. Joo, Q. H. Park, H. Ihee, B. Kim, *J. Am. Chem. Soc.* **2009**, *131*, 758.
- [23] X. G. Hu, W. L. Cheng, T. Wang, Y. L. Wang, E. K. Wang, S. J. Dong, *J. Phys. Chem. B* **2005**, *109*, 19385.
- [24] W. L. Zhai, D. W. Li, L. L. Qu, J. S. Fossey, Y. T. Long, *Nanoscale* **2012**, *4*, 137.
- [25] P. Li, Y. Li, Z.-K. Zhou, S. Tang, X.-F. Yu, S. Xiao, Z. Wu, Q. Xiao, Y. Zhao, H. Wang, P. K. Chu, *Adv. Mater.* **2016**, *28*, 2511.
- [26] J. Zaumseil, M. A. Meitl, J. W. P. Hsu, B. R. Acharya, K. W. Baldwin, Y. L. Loo, J. A. Rogers, *Nano Lett.* **2003**, *3*, 1223.
- [27] J. E. Green, J. W. Choi, A. Boukai, Y. Bunimovich, E. Johnston-Halperin, E. Delonno, Y. Luo, B. A. Sheriff, K. Xu, Y. S. Shin, H. R. Tseng, J. F. Stoddart, J. R. Heath, *Nature* **2007**, *445*, 414.
- [28] C. Kuegeler, M. Meier, R. Rosezin, S. Gilles, R. Waser, *Solid State Electron* **2009**, *53*, 1287.

- [29] B. Lu, V. Elofsson, E. P. Munger, K. Sarakinos, *Appl. Phys. Lett.* **2014**, 105.
- [30] W. Lee, S. Y. Lee, R. M. Briber, O. Rabin, *Adv. Funct. Mater.* **2011**, 21, 3424.
- [31] J. M. Montgomery, A. Imre, U. Welp, V. Vlasko-Vlasov, S. K. Gray, *Opt. Express* **2009**, 17, 8669.
- [32] X. H. Li, W. C. H. Choy, X. G. Ren, D. Zhang, H. F. Lu, *Adv. Funct. Mater.* **2014**, 24, 3114.
- [33] V. Mizeikis, E. Kowalska, S. Juodkazis, *J. Nanosci. Nanotechnol.* **2011**, 11, 2814.
- [34] J. Xu, P. Kvasnička, M. Idso, R. W. Jordan, H. Gong, J. Homola, Q. Yu, *Opt. Express* **2011**, 19, 20493.
- [35] A. D. McFarland, M. A. Young, J. A. Dieringer, R. P. Van Duyne, *J. Phys. Chem. B* **2005**, 109, 11279.
- [36] S. Dinda, V. Suresh, P. Thoniyot, A. Balcytis, S. Juodkazis, S. Krishnamoorthy, *ACS Appl. Mater. Interfaces* **2015**, 7, 27661.
- [37] S.-Y. Wang, X.-X. Jiang, T.-T. Xu, X.-P. Wei, S.-T. Lee, Y. He, *Appl. Phys. Lett.* **2014**, 104, 243104.
- [38] L. Scarabelli, M. Coronado-Puchau, J. J. Giner-Casares, J. Langer, L. M. Liz-Marzan, *ACS Nano* **2014**, 8, 5833.
- [39] J. A. Huang, Y. Q. Zhao, X. J. Zhang, L. F. He, T. L. Wong, Y. S. Chui, W. J. Zhang, S. T. Lee, *Nano Lett.* **2013**, 13, 5039.
- [40] H. W. Liu, L. Zhang, X. Y. Lang, Y. Yamaguchi, H. S. Iwasaki, Y. S. Inouye, Q. K. Xue, M. W. Chen, *Sci. Rep.* **2011**, 1.
- [41] Y. J. Oh, K. H. Jeong, *Adv. Mater.* **2012**, 24, 2234.
- [42] M. S. Schmidt, J. Hubner, A. Boisen, *Adv. Mater.* **2012**, 24, Op11.
- [43] P. Wang, O. Liang, W. Zhang, T. Schroeder, Y. H. Xie, *Adv. Mater.* **2013**, 25, 4918.
- [44] X. L. Zhu, L. Shi, M. S. Schmidt, A. Boisen, O. Hansen, J. Zi, S. S. Xiao, N. A. Mortensen, *Nano Lett.* **2013**, 13, 4690.
- [45] P. Wang, W. Zhang, O. Liang, M. Pantoja, J. Katzer, T. Schroeder, Y. H. Xie, *ACS Nano* **2012**, 6, 6244.
- [46] W. G. Xu, J. Q. Xiao, Y. F. Chen, Y. B. Chen, X. Ling, J. Zhang, *Adv. Mater.* **2013**, 25, 928.
- [47] S. Su, C. Zhang, L. H. Yuwen, J. Chao, X. L. Zuo, X. F. Liu, C. Y. Song, C. H. Fan, L. H. Wang, *ACS Appl. Mater. Interfaces* **2014**, 6, 18735.
- [48] Y. Lin, C. E. Bunker, K. A. S. Fernando, J. W. Connell, *ACS Appl. Mater. Interfaces* **2012**, 4, 1110.
- [49] Q. R. Cai, L. H. Li, Y. L. Yu, Y. Liu, S. M. Huang, Y. Chen, K. Watanabe, T. Taniguchi, *Phys. Chem. Chem. Phys.* **2015**, 17, 7761.
- [50] Q. Z. Hao, B. Wang, J. A. Bossard, B. Kiraly, Y. Zeng, I. K. Chiang, L. Jensen, D. H. Werner, T. J. Huang, *J. Phys. Chem. C* **2012**, 116, 7249.
- [51] W. Xie, P. H. Qiu, C. B. Mao, *J. Mater. Chem.* **2011**, 21, 5190.
- [52] R. A. Tripp, R. A. Dluhy, Y. P. Zhao, *Nano Today* **2008**, 3, 31.
- [53] O. Lyandres, N. C. Shah, C. R. Yonzon, J. T. Walsh, M. R. Glucksberg, R. P. Van Duyne, *Anal. Chem.* **2005**, 77, 6134.
- [54] K. E. Shafer-Peltier, C. L. Haynes, M. R. Glucksberg, R. P. Van Duyne, *J. Am. Chem. Soc.* **2003**, 125, 588.
- [55] M. Rycenga, J. M. McLellan, Y. N. Xia, *Chem. Phys. Lett.* **2008**, 463, 166.
- [56] W. C. Shih, K. L. Bechtel, M. V. Rebec, *J. Biomed. Opt.* **2015**, 20, 051036.
- [57] C. E. F. do Amaral, B. Wolf, *Med. Eng. Phys.* **2008**, 30, 541.
- [58] S. K. Vashist, *Anal. Chim. Acta* **2012**, 750, 16.
- [59] D. K. Sen, G. S. Sarin, *Brit. J. Ophthalmol.* **1980**, 64, 693.
- [60] V. K. Gupta, N. Atar, M. L. Yola, M. Eryilmaz, H. Torul, U. Tamer, I. H. Boyaci, Z. Ustundag, *J. Colloid Interface Sci.* **2013**, 406, 231.
- [61] C. Brouillette, W. Smith, M. Donahue, H. Huang, C. Shende, A. Sengupta, F. Inscore, M. Patient, S. Farquharson, *J. Biomed. Opt.*, **2012**, 20, 051036.